Available online at www.sciencedirect.com
ScienceDirect
Sensors and Actuators A 136 (2007) 496–503
SENSORS AND ACTUATORS A PHYSICAL
www.elsevier.com/locate/sna

Dynamic characterization of a linear electrostatic micromotor supported on microball bearings

Nima Ghalichechian [a], Alireza Modafe [a], Jeffrey H Lang [b], Reza Ghodssi [a,*]

[a] *MEMS Sensors and Actuators Lab (MSAL), Department of Electrical and Computer Engineering, Institute for Systems Research, University of Maryland, College Park 20742, MD, USA*

[b] *Department of Electrical Engineering and Computer Science, Massachusetts Institute of Technology, Cambridge, MA 02139, USA*

Received 17 July 2006; received in revised form 18 August 2006; accepted 21 August 2006
Available online 25 September 2006

Abstract

We report the dynamic characterization of a six-phase, bottom-drive, linear, variable-capacitance micromotor (B-LVCM) supported on microball bearings. The B-LVCM was fabricated and tested using a new test-bed. The motion of the micromotor was captured using low- and high-speed video cameras, tracked using image processing software, and analyzed to obtain the instantaneous velocity (11 mm/s), acceleration (1.9 m/s^2), and net force (0.19 mN) (all in amplitude) from the position data. The predicted (simulated) and measured net forces at different applied voltages are in good agreement. The micromotor was then modeled as a mass–spring–dashpot system and the lumped parameters were extracted from position measurement. This characterization methodology provides an understanding of the dynamic behavior of both the variable-capacitance micromachines and the microball bearings on which they are supported.

Keywords: Micromotor; Microball bearing; Variable-capacitance; Characterization

1. Introduction

Micromotors are a subset of power microelectromechanical systems (MEMS) that convert electrical energy to mechanical energy. Micromotors can be used for developing microsurgery instruments [1,2], such as endoscopes [3], as well as developing micropumps and microvalves with numerous applications (from delivery of fuel and biological samples, to cooling and analytical instruments [4–7]). Micromotors can also be employed in microassembly [8], micropropulsion, and microactuation [9,10].

Microball-bearing technology in silicon provides a reliable and robust support mechanism for the rotor of micromotors and microgenerators. Design and fabrication of the first-generation device, a three-phase, bottom-drive, linear, variable-capacitance micromotor (B-LVCM) supported on microball bearings, was demonstrated in our previous work [11]. The primary application of the B-LVCM (shown in Fig. 1) is long-range, high-speed, linear micropositioning. In addition, this device provides a platform to develop a rotary micromotor and investigate the mechanical properties of roller bearings in microelectromechanical systems (MEMS). The detailed design and fabrication, as well as initial test results for a six-phase B-LVCM were recently reported [12,13]. The electrical isolation of the electrodes from the silicon substrate in the first-generation device was achieved by the novel fabrication process *Embedded BCB in Silicon* (*EBiS*) to develop planarized isolated islands of low-*k* benzocyclobutene (BCB) polymer in the substrate [14]. Electrical isolation of motor electrodes and the substrate using a 30 μm thick low-*k* dielectric reduces the parasitic capacitances of the B-LVCM by more than 40% compared to a 10 μm thick (crack free) SiO_2.

The development of the linear micromotor is based on several studies of the motor core components. A vision-based in situ non-contact experimental system was developed to study the frictional behavior of the microballs in the microscale regime. Static and dynamic coefficient of friction (COF) of stainless steel microballs and the silicon grooves, fabricated by anisotropic silicon etching, were measured to be 0.01 and 0.007, respectively [15]. This is compared to 0.01–0.08 reported for silicon–silicon structures [16,17]. An infrared imaging was used to observe

* Corresponding author. Tel.: +1 3014058158; fax: +1 3013149281.
E-mail address: ghodssi@eng.umd.edu (R. Ghodssi).

0924-4247/$ – see front matter © 2006 Elsevier B.V. All rights reserved.
doi:10.1016/j.sna.2006.08.019

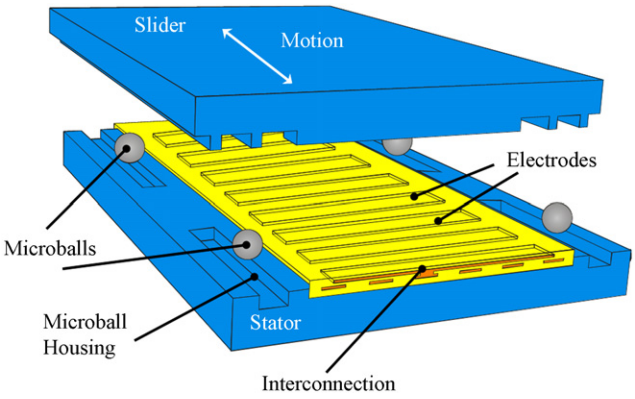

Fig. 1. Schematic 3D view of the bottom-drive, linear, variable-capacitance micromotor [11].

(through silicon) the dynamics of the stainless steel microballs and track their motion [18]. It was verified that the microballs roll most of the time with occasional sliding and collisions. The algorithm for extracting the COF was later modified to reduce the noise of position data; the measured frictional force demonstrated a viscoelastic behavior [19]. The COF-velocity characteristic was modeled as a *Langevin Function* which showed a linear relation for a [−0.1, 0.1 m/s] velocity range.

The relative permittivity and breakdown voltage of BCB low-*k* polymer, used as an electrical insulator for reducing parasitic losses of the micromachine, were measured and the effect of humidity on these properties was studied [20]. The relative permittivity of BCB was measured to be 2.49 in dry environment and was only increased by 1.2% after a humidity stress test of 85% RH at 85 °C. The study on the *I–V* characteristics of BCB showed that humidity stress reduces the breakdown strength by 2–3-fold and increases the maximum leakage current by 10-fold. The integration of a BCB film with conventional MEMS fabrication technologies was also demonstrated. A fabrication process was developed for integration of a 1 μm thick BCB film and 200 μm deep anisotropically etched grooves in silicon with potassium hydroxide (KOH) [21,22]. The process involved the adhesion improvement of BCB and metal layers. In order to understand the mechanism of the adhesion improvement, the interface of BCB and the metal layer was analyzed using secondary ion mass spectroscopy (SIMS) and Auger electron spectroscopy (AES) [22–24]. Adhesion properties of BCB to chromium (Cr) and gold (Au) layers were correlated to the interface chemistry and diffusion of carbon (C) and silicon (Si) at the polymer/metal interface.

This paper reports our latest results on the dynamic characterization of the linear variable-capacitance micromotor supported on microball bearings. The design and fabrication of the second-generation B-LVCM are described in the Sections 2 and 3, respectively. The test setup used for the characterization of the devcie is introduced in Section 4. The dynamic characterization of the six-phase micromotor, including the measurement results of position, instantaneous velocity, acceleration, and the net force on the slider [25], are presented in Section 5. The device is then modeled with a simple mass–dashpot–spring system. The model parameters were extracted from the measurement data. Test and modeling results are compared and discussed in Section 6.

2. Design

Fig. 1 shows a 3D exploded view of the linear micromotor supported on microball bearings. B-LVCM is comprised of three major components: stator, slider, and microballs. Two new technologies were implemented in the development of the linear micromachine: (1) microball bearing in silicon as a support mechanism and (2) BCB low-*k* polymer as an insulating layer [11,12].

Unlike the conventional variable-capacitance micromotors (VCMs) that were side-drive [26–30], this micromotor has a bottom-drive design which increases the active area and force of the motor. The microball-bearing design provides the mechanical support for maintaining a uniform air gap that was difficult to maintain in conventional (side-drive or top-drive) VCMs with center-pin or flange designs. The center-pin design results in friction, wear, fracture, stiction, and contamination-based failure modes [31].

The fabrication process of the microball-bearing-supported machine is less complex than gas-lubricated machines [32] and the rotor operation is more reliable and stable. The microball-bearing technology results in stable, robust, and reliable mechanical support that was not possible using other technologies.

The second core technology developed for the B-LVCM is a thick, low-*k*, isolating layer. The conventional dielectric film of silicon dioxide (SiO_2) with relative permittivity of $k = 3.9$ was replaced by a thick low-*k* BCB polymer with $k = 2.65$ in B-LVCM. This results in a reduction of parasitic capacitance and an increase in efficiency of the motor. BCB also exhibits less residual stress (∼28 MPa-tensile) than SiO_2 and can be deposited up to 26 μm thick in a single coating step; therefore, a micromachine with BCB film has less curvature and the air gap, one of the most critical design parameters, is more uniform. Considering the large size of the micromotor, this is a significant advantage. The geometry specifications of the tested B-LVCM are shown in Table 1. The micromotor has an electrode-to-pole ratio of 6:4 with identical electrode and pole width of 90 μm. The properties of the microballs (Thomson Precision Ball Company) used in this study are shown in Table 2.

Table 1
Micromotor geometry specifications (electrodes refer to the stator and poles refer to the salient structures on the slider)

Parameter	Value
Electrode/pole width (μm)	90/90
Electrode/pole spacing (μm)	30/90
Electrode/pole number	84/36
Air gap (μm)	26–34
Microball housing width (μm)	290
Microball housing length (mm)	3.9
Stator length/width (mm)	14/10
Slider length/width (mm)	12/10

Table 2
Microball specifications

Property	Value
Material	440C stainless steel
Material composition (%)	Chromium: 16–18, Carbon: 0.95–1.20
Modulus of elasticity (GPa)	199
Yield strength (GPa)	1.89
Knoop hardness (kg/mm^2)	660
Density (10^3 kg/m^3)	7.6
Diameter (μm)	284.5
Tolerance (μm)	0.25
Surface roughness (nm)	25.4

3. Fabrication

The second-generation B-LVCM was fabricated with major modifications to the process of the first-generation [13] device. The fabrication process of the stator uses seven mask levels and involves the deposition and patterning of three BCB layers, two metal layers, and etching of microball housings in silicon. The schematic cross section of the stator is shown in Fig. 2. The first metal layer forms the interconnection level that connects every other sixth electrode of the six-phase micromachine whereas the second metal layer forms the electrode level. The three BCB layers provide electrical isolation between metal layers as well as isolation of metal layers from substrate and air.

First, a 3 μm thick photosensitive BCB (Cyclotene 4024-40 from Dow Chemical, Midland, MI, USA) is spun, patterned, and partially cured (at 210 °C for 50 min). In the first-generation device [13], this step was comprised of a silicon etch step using deep reactive ion etching (DRIE) and multiple photolithography and chemical mechanical planarization (CMP) steps. For simplicity, those steps were replaced by a 3 μm thick BCB deposition. A 20/250 nm thick Cr/Au metal layer (interconnection) is then sputtered and patterned using a positive photoresist (Shipley 1813) and wet etching. The yield of the Cr/Au metallization process was increased by replacing the original lift-off process in the first-generation device with an etch process. A dielectric layer (Cyclotene 4024-40) with a thickness of 3.2 μm is then spun, patterned, and partially cured (at 210 °C for 50 min) to form an interlayer dielectric (ILD) with open vias for electrical connection between the two metal layers. The partial cure of the BCB results in 75% polymerization and a better adhesion to the metal layers [22]. The second metal layer (electrode) with 20/250 nm thick Cr/Au layer is patterned using photolithography with an

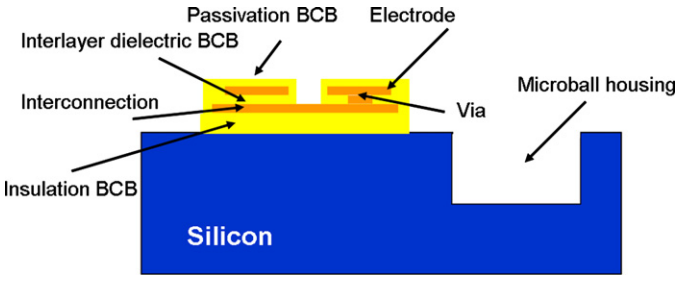

Fig. 2. Schematic cross section of the B-LVCM stator with three dielectric and two metal layers (dimensions are not to scale).

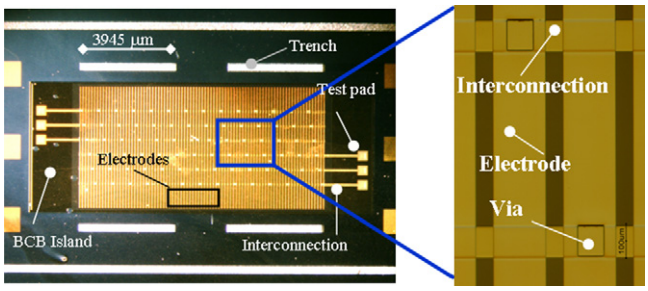

Fig. 3. Optical micrograph (top view) of the six-phase stator comprises three BCB layers, two metal layers, and four trenches for housing microballs.

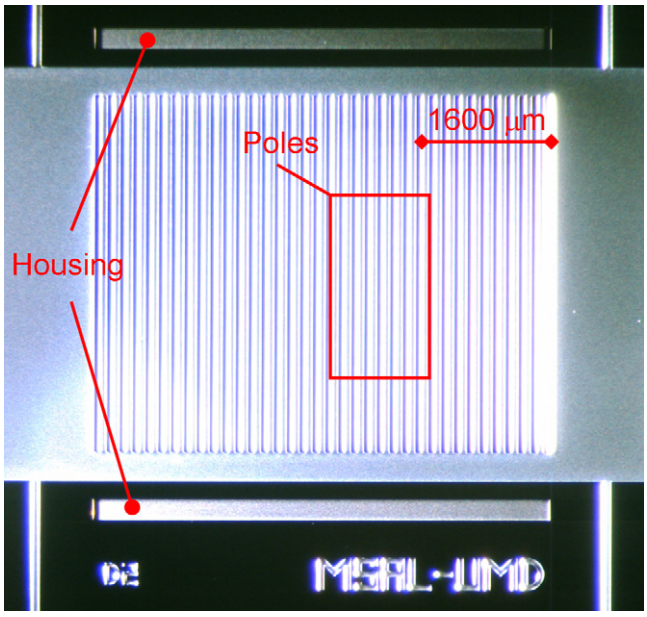

Fig. 4. Optical micrograph (top view) of the slider showing poles and microball housing etched into silicon substrate using DRIE.

image reversal photoresist (AZ5214E), sputtering, and lift-off in acetone. A 2.1 μm thick passivation layer (Cyclotene 4022-35) is then spun, patterned, and fully cured (at 250 °C for 1 h). This is followed by the patterning and etching of silicon (130 μm deep) using a 9 μm thick positive photoresist (AZ9245) and DRIE to form the microball housings.

The slider fabrication process is comprised of a lithography step and a DRIE step to etch microball housing and poles simultaneously. Figs. 3 and 4 show the fabricated stator and slider of the six-phase micromotor, respectively. The assembly of the micromotor requires the manual placement of the microballs in the stator trenches using a pair of tweezers. The slider is then aligned with the stator and positioned on top of the microballs.

4. Test setup

A new test-bed for the characterization of the micromotor was developed. Fig. 5 shows the block diagram of the test station consist of a six-channel, high-voltage excitation system, a high-speed camera, and an image processing unit. Initially, the motion of the motor was captured using a 30-frame-per-second (fps) camera. The speed of a standard 30-fps camera was found

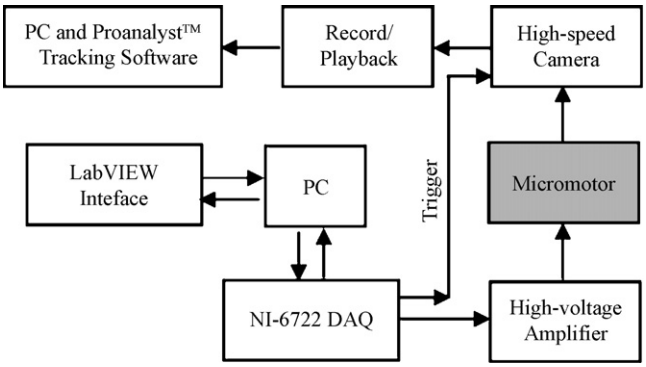

Fig. 5. Block diagram of the micromotor test station.

to be too low for capturing the transient response of the micromotor. Therefore, real-time measurement was performed using a low-noise, monochromatic, high-speed (635–1000 fps) video camera with 1280 × 1024 pixels (MotionPro HS-3 from Redlake, Tucson, AZ, USA) and a long-distance, microscopic lens system (Model KV from Infinity Photo-Optical, Boulder, CO, USA). This real-time measurement method was preferred over conventional stroboscopic dynamometry techniques previously used for side-drive micromotors [33] because of the greater displacement and temporal accuracy.

5. Results

The micromotor is excited with six square-wave pulses. The first three phases are 120° out of phase. The remaining three phases are the inverse of the first three. This excitation configuration with equal number of positive and negative applied potentials prevents charge build-up on the slider. Figs. 6 and 7 show the displacement of the slider measured for excitation frequencies (f_e) of 10 and 20 Hz, respectively, at a capture rate of 30 fps. Since the range of motion in this design is limited to 3.6 mm, the direction of motion is changed (forward and backward) at a frequency of $f_d = 1.5$ Hz. This is accomplished by switching the sequence of the phases. The value of f_d is chosen

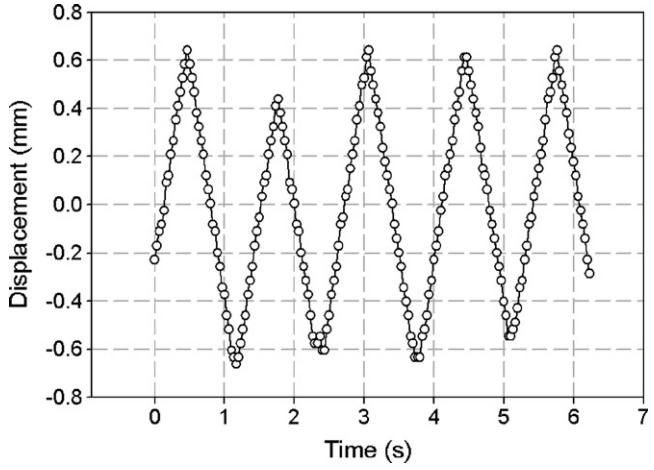

Fig. 6. Displacement of the slider when excited with 120 V, 10 Hz, six-phase, square pulses and measured using a 30-fps camera. The direction of the motion alternates with $f_d = 1.5$ Hz.

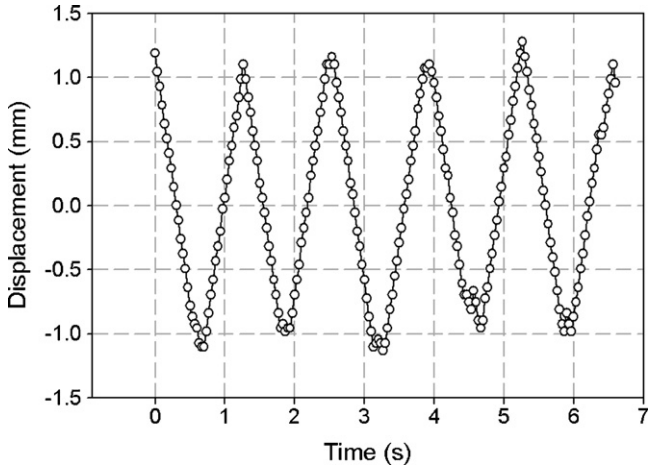

Fig. 7. Displacement of the slider when excited by 120 V, 20 Hz, six-phase, square pulses and measured using a 30-fps camera ($f_d = 1.5$ Hz).

such that the direction of the slider motion is changed before it reaches the end of the microball housing. The saw-tooth profile, observed in Figs. 6 and 7, is a result of the change in the direction of the motion.

The theoretical average velocity (V_{avg}) of the slider is given by

$$V_{avg} = 2wf_e \quad (1)$$

where w is the width of an electrode or pole and f_e is the frequency of excitation voltage [13]. The average velocity can be determined from the slopes of the ramps in the two graphs (Figs. 6 and 7). Similar measurements were performed at 40 and 80 Hz excitation frequencies. The results, summarized in Table 3, show a good agreement between predicted (from Eq. (1)) and measured values of V_{avg} for $f_e \leq 60$ Hz.

The transient response of the micromotor to 120 V square pulses and excitation frequency of $f_e = 10$ Hz was measured at 1000 fps while the camera's capture sequence was synchronized to the excitation voltage. Fig. 8 shows the acceleration of the slider from rest position to a quasi-steady-state in approximately 20 ms (first region). After this period the machine continues with an average velocity of V_{avg} (second region), however, the instantaneous acceleration is not zero and the velocity changes around the average.

Fig. 9 shows the oscillation of the slider position, $X(t)$, in a 130 ms window captured at 635 fps ($V = 120$ V, $f_e = 10$ Hz). This is similar to Fig. 8, except that the lower capture rate was used to facilitate faster image and data processing. Fig. 9 shows a time window that was arbitrary chosen from the operation phase of the

Table 3
Comparison of predicted and measured average velocity of the micromotor

Excitation frequency (Hz)	Predicted average velocity (mm/s)	Measured average velocity (mm/s)
10	1.80	1.94 ± 0.02
20	3.60	3.98 ± 0.02
40	7.20	7.37 ± 0.12
80	14.40	7.21–11.10

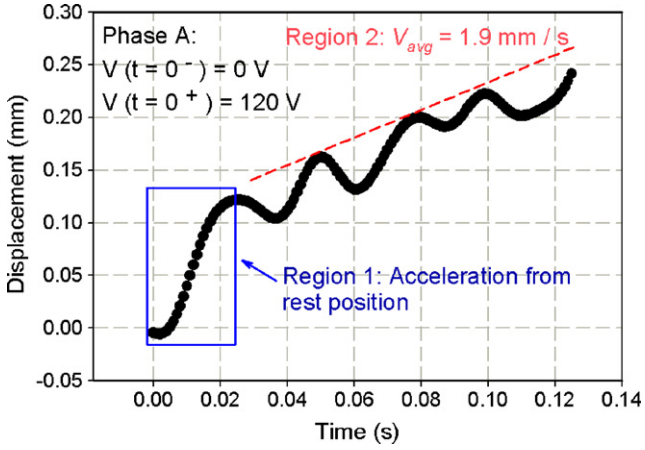

Fig. 8. Startup of the micromotor from rest position captured with a 1000-fps camera showing two regions of operation: (1) acceleration from rest position and (2) quasi-steady-state operation with an average velocity of V_{avg} and local oscillations.

machine. In order to study the transient response of the machine, the linear component of the displacement signal, $V_{avg} \times t$, was filtered out from the graph in Fig. 9 and the remaining component, $x(t) = X(t) - (V_{avg} \times t)$, which shows the local oscillation of the displacement, was plotted in Fig. 10. A damped sinusoidal transient response of the slider motion can be seen in this figure. The instantaneous velocity and acceleration were computed from the first and second derivatives of the fitted curve (red curve in Fig. 10) and are shown in Figs. 11 and 12, respectively. The average velocity of 1.9 mm/s observed in Fig. 11 is similar to the low-speed measurement results from a 30-fps camera. Furthermore, Fig. 12 demonstrates the instantaneous net force on a 0.1 g slider (plotted on the right axis). This net force is the difference between lossless electrostatic and frictional forces that are discussed in the next section. Similarly, Fig. 13 shows the acceleration and the net force measured with the applied voltage of 150 V. As expected, the net force at 150 V is increased by a ratio of $(150/120)^2 = 1.56$ from the force measured at 120 V. The results show an excellent agreement between the measured and predicted values.

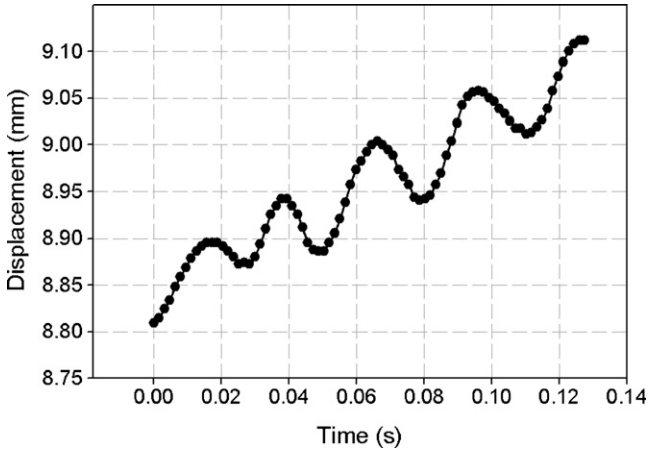

Fig. 9. Position of the slider, $X(t)$, in a 130 ms time window captured at 635 fps shows an average speed of 1.9 mm/s at 10 Hz excitation, as well as a sinusoidal oscillation.

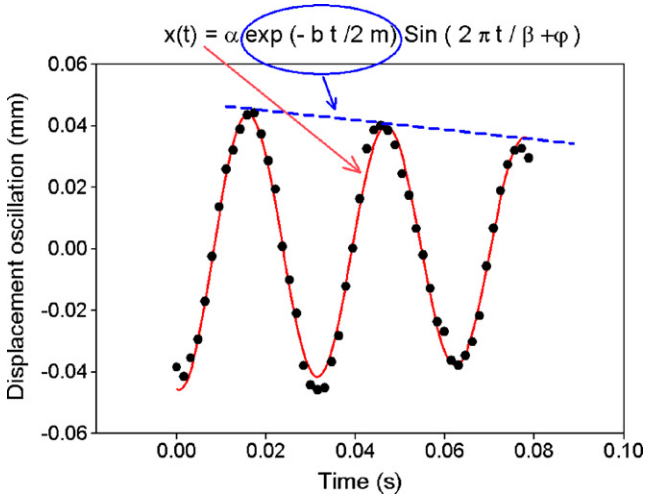

Fig. 10. Local slider displacement, $x(t) = X(t) - (V_{avg} \times t)$, measured at 635 fps shows damped sinusoidal transient response. The standard coefficient of determination (R^2) was calculated to be 0.9876 ($V = 120$ V).

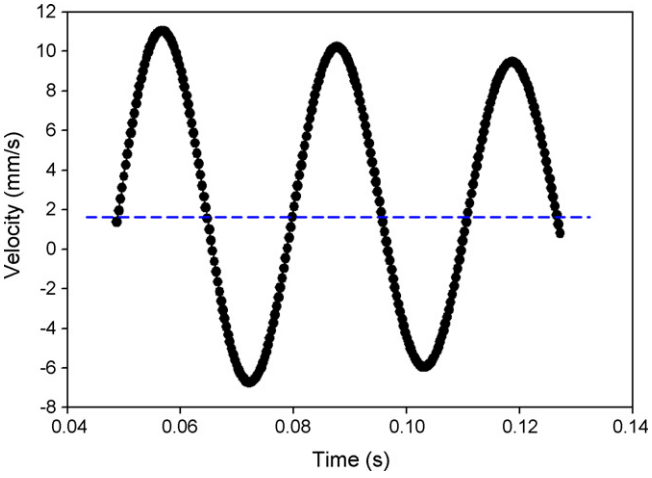

Fig. 11. Instantaneous velocity of the slider at $V = 120$ V with damped sinusoidal form was computed from the curve fit to the position data (Fig. 10). The average velocity is 1.9 mm/s.

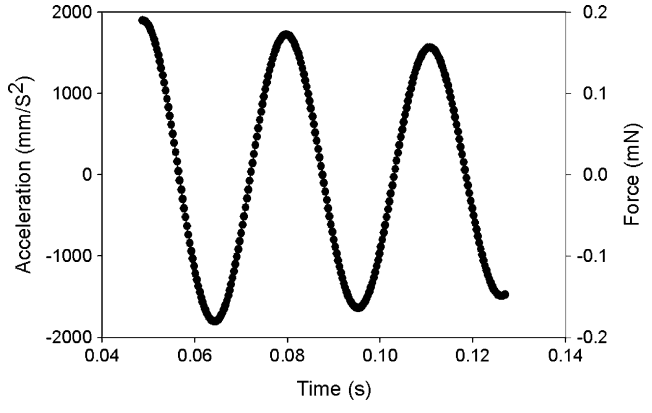

Fig. 12. Measured instantaneous acceleration (left axis) and the net force (right axis) of the 0.1 g slider with excitation voltage of $V = 120$ V were computed from the velocity data shown in Fig. 11.

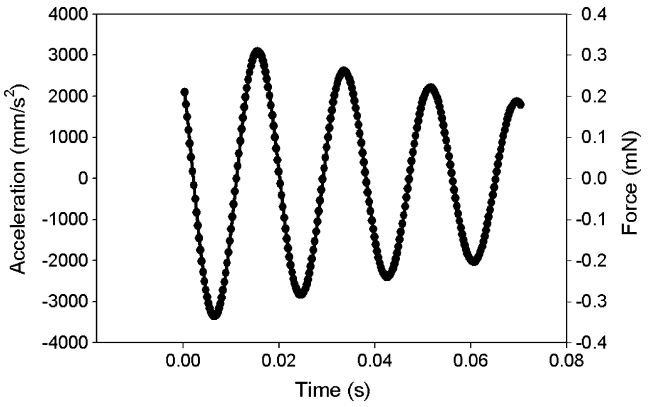

Fig. 13. Measured instantaneous acceleration (left axis) and the net force (right axis) of the slider with excitation voltage of $V = 150$ V shows a 1.57-fold increase in the net force compared to $V = 120$ V excitation.

6. Modeling

The force measurement results, discussed earlier, can be compared to the force of a lossless system obtained from finite element simulations. The aligning force of the slider can be written as

$$F_{\mathrm{Ph}} = \frac{1}{2} V_{\mathrm{Ph}}^2 \frac{\partial C_{\mathrm{Ph}}}{\partial x} \tag{2}$$

where F_{Ph} is the aligning force generated by each phase, V_{Ph} the amplitude of the applied voltage, C_{Ph} the capacitance of each phase, and x is the position of the slider [13]. Therefore, the aligning force at a given voltage can be derived from the capacitance variations. These data were obtained from finite element simulation using FEMLAB.

Fig. 14 shows the simulation results of the machine capacitance with the electrode width and the air gap of 90 and 10 μm, respectively. The capacitance of the first three phases, shown in Fig. 14, can be numerically differentiated to obtain the total aligning force of the six-phase micromotor. The remaining three phases (not shown in Fig. 14) have identical capacitance profiles. Fig. 15 shows the numerical differentiation of the capacitance

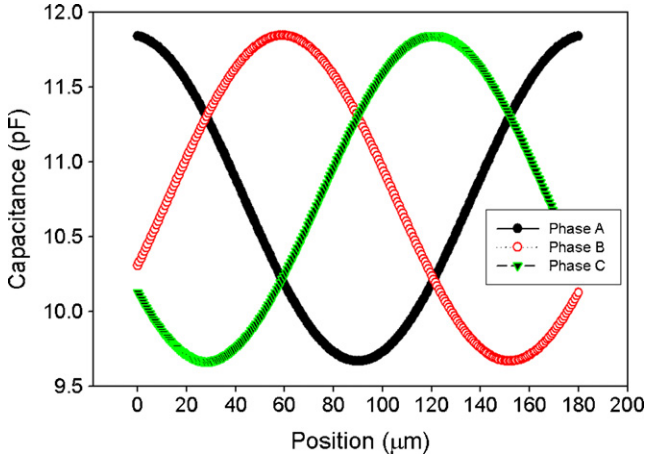

Fig. 14. Finite element simulation results of the B-LVCM capacitance vs. position for the first three phases.

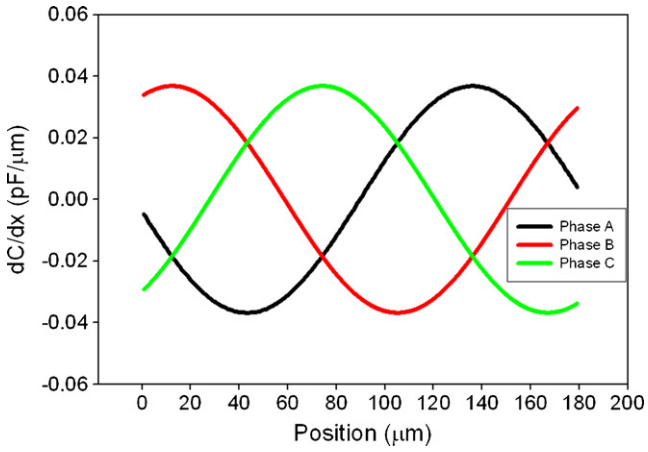

Fig. 15. Numerical differentiation results of capacitance vs. slider displacement.

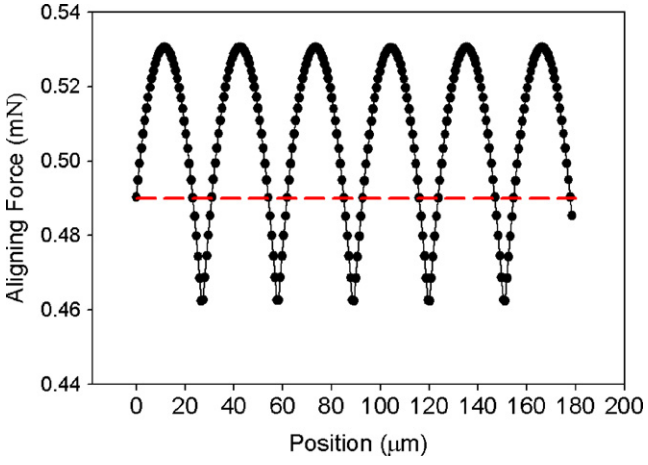

Fig. 16. Total aligning force of the six-phase micromotor at $V = 120$ V extracted from the simulation data.

of the first three phases versus slider displacement. Fig. 16 illustrates the extracted aligning force versus position (x) and its average value with a 120 V excitation calculated from Fig. 15 and Eq. (2). This aligning force, which represents the total electrostatic force (without considering any electrical or mechanical losses), is comparable to (but slightly larger than) the net force obtained in our experiment.

The measurement results shown in Fig. 10 are used to model the dynamics of the system and extract the model parameters of the micromotor. The B-LVCM was modeled with a simple mass–dashpot–spring system as shown in Fig. 17. Such a system

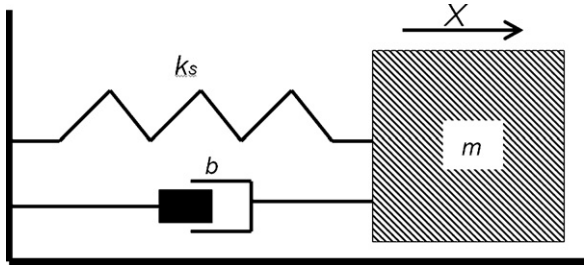

Fig. 17. Simplified model of the micromotor represented by a mass–dashpot–spring system.

is described by the 2nd order differential equation:

$$m\frac{d^2x}{dt^2} + b\frac{dx}{dt} + k_s x = 0 \quad (3)$$

where m is the mass of the slider, b a dashpot coefficient representing the friction of microballs and silicon housing, and k_s represents the (electrostatic) spring constant of the electrode-pole variable capacitors. Eq. (3) describes the dynamic response of the B-LVCM in absence of any external force. The under-damped solution for such a system can be written as

$$x(t) = A\exp\left(\frac{-b}{2m}t\right)\sin(\omega_d t + \phi) \quad (4)$$

where A and ϕ are constant values and

$$\omega_d = \sqrt{\frac{k_s}{m} - \frac{b^2}{4m^2}} \quad (5)$$

The values for b and k_s can be extracted from the measurement of the displacement decay ($\exp(-b/2m)t$) and displacement period $T_d = 2\pi/\omega_d$ shown in Fig. 10. The dashpot coefficient values (b) were found to be 6.25×10^{-4} and 2.0×10^{-3} kg/s at $V = 120$ and 150 V, respectively. Furthermore, the (electrostatic) spring constant values (k_s), extracted from the period of displacement data, were found to be 4.3 and 30.4 N/m at $V = 120$ and 150 V, respectively.

7. Discussion

The results from the position measurement using a 30-fps camera, summarized in Table 3, show a good agreement between predicted and measured values of the average velocity for the excitation frequency of $f_e \leq 60$ Hz. However, the motor does not pull into synchronization at 80 Hz or higher. This phenomenon is not due to the limited range of the linear motion (3.6 mm) nor the change in the direction of motion. Fig. 8 shows that B-LVCM is capable of synchronizing in about 20 ms. Therefore, the lack of synchronization at higher excitation frequencies is due solely to the open-loop excitation of this synchronous micromotor and is expected to be addressed with a closed-loop excitation configuration which is out of the scope of this paper.

The period of the oscillations in the transient response measurements (Figs. 8–13) was found to be independent of the frequency of excitation voltage. It is believed that this period is determined mainly by the system characteristics such as slider mass, friction, and electrostatic spring constant of a variable-capacitance structure. The mass–dashpot–spring system presented earlier explains this behavior.

The mass of the slider was calculated from the volume of the slider and density of silicon to be 0.1 g. The measured net force, shown in Figs. 12–13, is the result of the electrostatic force, produced by the micromachine, and the frictional force between microball bearings and the silicon housing. This force (Figs. 12–13) was verified to be proportional to the square of voltage. It can be seen that the measured net force (Fig. 12) is less than the average aligning force obtained from simulation (Fig. 16). The friction force is calculated from the difference between measured and simulated forces. The friction force is a function of the normal force on the slider and, therefore, changes with slider position. The coefficient of friction, which is defined as the ratio of the frictional and normal forces, can be extracted provided that the position-depending normal force is calculated. An analytical approach to evaluate the change in the normal force with the slider position will be pursued in future. However, an alternative method for understanding the role of the friction was presented in Section 6.

The presented mass–spring–dashpot model is a valuable tool to understand the dynamics of the micromotor including electrostatic and frictional behavior. The increase in the dashpot coefficient (b) with increase in the excitation voltage is due to the increase in the normal force. As mentioned earlier, b is a coefficient which represents the frictional force on the slider. This force is proportional to the normal force on the slider and is increased with the increase in the applied voltage. Another extracted parameter is the electrostatic spring constant (k_s). For simplicity, k_s was chosen to be independent of the slider position (x). Furthermore, the spring constant value, which increases with the increase in the applied voltage, is also a function of device capacitance and slider position. The mass–dashpot–spring model was proven to be a simple and suitable tool for extracting device parameters. Non-linear effects, such as position dependency of the electrostatic spring, velocity dependency of the friction force, and the microscale tribological effects (adhesion and hysteresis) were considered to be negligible. The modeling results show that the micromotor is well represented with a second-order linear system.

8. Conclusion

The dynamic characterization of a six-phase, bottom-drive, linear, variable-capacitance micromotor (B-LVCM) supported on microball bearings was presented. A new generation of the micromotor was fabricated and tested. The slider position of the B-LVCM was measured using low- and high-speed video cameras; the instantaneous and average velocity, acceleration, and net force were extracted from the position measurement. Considering the effect of frictional force in the operation of the micromotor, the measured force (0.2 mN peak) is in good agreement with the simulated force (0.53 mN peak). The transient response of the micromotor to square-pulse excitation was analyzed.

The B-LVCM was modeled with a mass–spring–dashpot system; the dashpot coefficient and electrostatic spring constant were extracted from measurement results at two different actuation voltages. The evaluation of these two values (b and k_s), for different micromotors with distinct electrical or mechanical designs, enables us to determine the optimum design for a given application. The characterization methodology presented in this paper is applicable to a wide range of micromachines and provides useful information for design, control, and understanding the dynamic behavior of micromachines.

Acknowledgments

This work was supported by the Army Research Lab under Grant No. CA#W911NF-05-2-0026, Army Research Office through the MURI Program under Grant No. ARMY-W911NF0410176 with Dr. Tom Doligalski as the technical monitor, and the National Science Foundation under Grant No. ECS-0224361. The authors would also like to thank Mr. Thomas Loughran, Jonathan Hummel, and James O'Connor from the University of Maryland (UMD) clean room facilities (FabLab) for their help with the fabrication of devices, as well as Mr. Alex Frey for his help with the test setup. The authors are also grateful to Professor Kenneth Kiger and Jungho Kim from Department of Mechanical Engineering, UMD for their help with the high-speed camera measurement.

References

[1] X. Wang, S. Cui, S. Cheng, Advantages of electrostatic micromotor and its application to medical instruments, in: Conference Record of the 2002 IEEE Industry Applications Conference, vol. 4, 37th IAS Annual Meeting, Pittsburgh, PA, USA, 2002, pp. 2466–2468.

[2] D. Polla, A. Erdman, D. Peichel, R. Rizq, Y. Gao, D. Markus, Precision micromotor for surgery, in: Proceedings of 1st Annual International IEEE-EMBS Special Topic Conference on Microtechnologies in Medicine and Biology, Lyon, France, October 12–14, 2000, pp. 180–183.

[3] L.M. Gao, Y. Chen, L.M. Lin, G.Z. Yan, Micro motor based new type of endoscope, in: Proceedings of the 20th Engineering in Medicine and Biology Society, Hong Kong, China, 1998, p. 1822.

[4] D.J. Laser, J.G. Santiago, A review of micropumps, J. Micromech. Microeng. 14 (2004) R35.

[5] T. Weisener, G. Vogele, M. Widmann, C. Bark, R.D. Schraft, A. Bertholds, A. Braunschweiler, Development and fabrication of a rotary micropump and its industrial and medical applications, in: Proceedings of the SPIE, Austin, TX, USA, 1996, pp. 218–225.

[6] C.H. Ahn, M.G. Allen, Fluid micropumps based on rotary magnetic actuators, in: IEEE Microelectromechanical Systems (MEMS '95), Amsterdam, Netherlands, 1995, p. 408.

[7] B. Mladen, J.M. Jack, P.G. Andrew, S. Schultz, Electromagnetic micromotor for microfluidics applications, Appl. Phys. Lett. 79 (2001) 1399–1401.

[8] S. Fatikow, A. Falzullin, J. Seyfried, Planning of a microassembly task in a flexible microrobot cell, in: Proceedings of the IEEE International Conference on Robotics and Automation (ICRA), San Francisco, CA, USA, April 24–28, 2000, p. 1121.

[9] R. Yeh, S. Hollar, K.S.J. Pister, Design of low-power silicon articulated microrobots, J. Micromechatronics 1 (2002) 191.

[10] R. Yeh, E.J.J. Kruglick, K.S.J. Pister, Surface-micromachined components for articulated microrobots, J. Microelectromech. Syst. 5 (1996) 10.

[11] A. Modafe, N. Ghalichechian, J.H. Lang, R. Ghodssi, A microball-bearing-supported linear electrostatic micromotor with benzocyclobutene polymer insulating layers, in: The 13th International Conference on Solid-State Sensors, Actuators, and Microsystems (Transducers '05), Seoul, Korea, 2005, pp. 693–696.

[12] A. Modafe, N. Ghalichechian, A. Frey, J.H. Lang, R. Ghodssi, Microball-bearing-supported electrostatic micromachines with polymer dielectric films for electromechanical power conversion, in: The Fifth International Workshop on Micro NanoTechnology for Power Generation and Energy Conversion Applications (Power MEMS '05), Tokyo, Japan, 2005, pp. 173–176.

[13] A. Modafe, N. Ghalichechian, A. Frey, J.H. Lang, R. Ghodssi, Microball-bearing-supported electrostatic micromachines with polymer dielectric films for electromechanical power conversion, J. Micromech. Microeng. 16 (2006) S182–S190.

[14] A. Modafe, N. Ghalichechian, M. Powers, M. Khbeis, R. Ghodssi, Embedded benzocyclobutene in silicon: an integrated fabrication process for electrical and thermal isolation in MEMS, Microelectron. Eng. 82 (2005) 154.

[15] T.W. Lin, A. Modafe, B. Shapiro, R. Ghodssi, Characterization of dynamic friction in MEMS-based microball bearings, IEEE Trans. Instrum. Meas. 53 (2004) 839–846.

[16] K. Deng, W.H. Ko, G.M. Michal, A preliminary study on friction measurements in MEMS, in: International Conference on Solid-State Sensors and Actuators, Digest of Technical Papers (TRANSDUCERS '91), San Francisco, CA, USA, 1991, p. 213.

[17] K. Noguchi, H. Fujita, M. Suzuki, N. Yoshimura, The measurements of friction on micromechatronics elements, in: IEEE Micro Electro Mechanical Systems (MEMS'91), Nara, Japan, 1991, p. 148.

[18] X. Tan, A. Modafe, R. Herger, N. Ghalichechian, B. Shapiro, J.S. Baras, R. Ghodssi, Vision-based microtribological characterization of linear mciroball bearings, in: Proceedings of the ASME/STLE International Joint Tribology Conference, Long Beach, CA, USA, October 24–27, 2004.

[19] X. Tan, A. Modafe, R. Ghodssi, Measurement and modeling of dynamic rolling friction in linear microball bearings, J. Dynamic Syst., Meas. Control, in press.

[20] A. Modafe, N. Ghalichechian, B. Kleber, R. Ghodssi, Electrical characterization of benzocyclobutene polymers for electric micro machines, IEEE Trans. Device Mater. Reliability 4 (2004) 495–508.

[21] N. Ghalichechian, A. Modafe, R. Ghodssi, Integration of silicon anisotropic wet etching and BCB processes, in: AVS 50th International Symposium, Baltimore, MD, USA, November 2–7, 2003.

[22] N. Ghalichechian, A. Modafe, R. Ghodssi, P. Lazzeri, V. Micheli, M. Anderle, Integration of benzocyclobutene polymers and silicon micromachined structures using anisotropic wet etching, J. Vac. Sci. Technol. B 22 (2004) 2439–3244.

[23] N. Ghalichechian, Integration of benzocyclobutene polymers and silicon micromachines structures fabricated with anisotropic wet etching, Master's Thesis, Department of Electrical and Computer Engineering, University of Maryland, College Park, MD, USA, 2004.

[24] N. Ghalichechian, A. Modafe, P. Lazzeri, V. Micheli, M. Anderle, R. Ghodssi, Characterization of benzocyclobutene and chromium-gold film interface for application in silicon micromachining, in: Material Research Society 2005 Spring Meeting, San Francisco, CA, USA, 28 March–April 1, 2005.

[25] N. Ghalichechian, A. Modafe, A. Frey, J.H. Lang, R. Ghodssi, Dynamic characterization of a linear variable-capacitance micromotor, in: Solid-State Sensor, Actuator, and Microsystems Workshop, Hilton Head Island, SC, USA, June 4–8, 2006, pp. 19–22.

[26] Y.C. Tai, L.S. Fan, R.S. Muller, IC processed micro-motors: design, technology, and testing, in: Proceedings of Micro Electro Mechanical Systems, Salt Lake City, UT, 1989, p. 1.

[27] M. Mehregany, K.J. Gabriel, W.S.N. Trimmer, Integrated fabrication of polysilicon mechanisms, IEEE Trans. Electron Devices 35 (1988) 719.

[28] M. Mehregany, Microfabricated silicon electric mechanisms, Ph.D. Thesis, Massachusetts Institute of Technology, Department of Electrical Engineering and Computer Science, Cambridge, MA, 1990.

[29] M. Mehregany, S.F. Bart, L.S. Tavrow, J.H. Lang, S.D. Senturia, Principles in design and microfabrication of variable-capacitance side-drive motors, J. Vac. Sci. Technol., A: Vac., Surf., and Films 8 (1990) 3614–3624.

[30] M. Mehregany, S.D. Senturia, J.H. Lang, P. Nagarkar, Micromotor fabrication, IEEE Trans. Electron Devices 39 (1992) 2060.

[31] W. Zhang, G. Meng, H. Li, Electrostatic micromotor and its reliability, Microelectron. Reliability 45 (2005) 1230.

[32] L.G. Frechette, S.A. Jacobson, K.S. Breuer, F.F. Ehrich, R. Ghodssi, R. Khanna, W. Chee Wei, Z. Xin, M.A. Schmidt, A.H. Epstein, High-speed microfabricated silicon turbomachinery and fluid film bearings, J. Microelectromech. Syst. 14 (2005) 141.

[33] S.F. Bart, M. Mehregany, L.S. Tavrow, J.H. Lang, S.D. Senturia, Electric micromotor dynamics, IEEE Trans. Electron Devices 39 (1992) 566.